Article
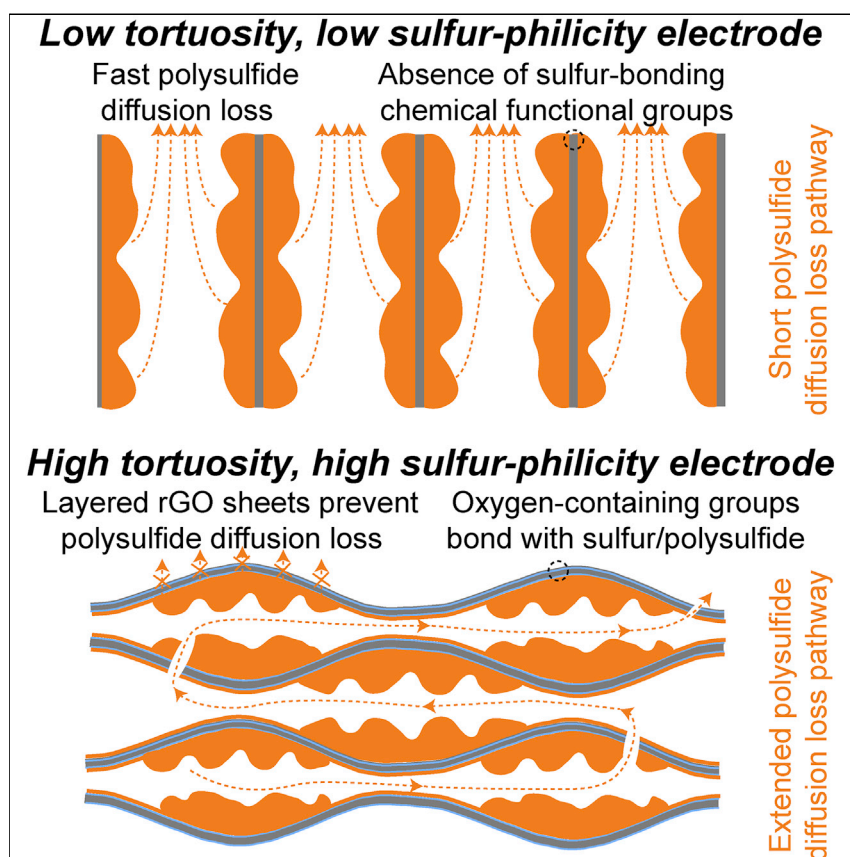
Electrode Design with Integration of High Tortuosity and Sulfur-Philicity for High-Performance Lithium-Sulfur Battery

Low tortuosity, low sulfur-philicity electrode

Fast polysulfide diffusion loss

Absence of sulfur-bonding chemical functional groups

Short polysulfide diffusion loss pathway

High tortuosity, high sulfur-philicity electrode

Layered rGO sheets prevent polysulfide diffusion loss

Oxygen-containing groups bond with sulfur/polysulfide

Extended polysulfide diffusion loss pathway

Hao Chen, Guangmin Zhou, David Boyle, ..., Wenxiao Huang, Yusheng Ye, Yi Cui

yicui@stanford.edu

HIGHLIGHTS

High tortuosity suppresses diffusion loss of polysulfide from sulfur cathode

High sulfur-philicity favors bonding sulfur-based materials within the electrode

Same graphene host suppresses Li dendrite growth in anode to prolong cycle life

Ultrahigh loading and ultrastable cycling under high-energy-density parameters

The Li-S battery is limited by diffusion loss of soluble polysulfide active materials in cathode and dendrite growth in anode. Here, we demonstrate an integrated concept of high electrode tortuosity and sulfur-philicity for thick sulfur cathode, extending the diffusion loss pathway of polysulfide and bonding with sulfur-based materials to localize the soluble polysulfide within the electrode. Utilizing this integrated design, ultrahigh cathode capacities and cycling stability are achieved. The same graphene host suppresses dendrite growth in Li anode, enabling 278% prolonged cycle life.

Improvement
Enhanced performance with innovative design or material control

5

CellPress

Article

Electrode Design with Integration of High Tortuosity and Sulfur-Philicity for High-Performance Lithium-Sulfur Battery

Hao Chen,[1] Guangmin Zhou,[1] David Boyle,[1] Jiayu Wan,[1] Hongxia Wang,[1] Dingchang Lin,[1] David Mackanic,[3] Zewen Zhang,[1] Sang Cheol Kim,[1] Hye Ryoung Lee,[1] Hansen Wang,[1] Wenxiao Huang,[1] Yusheng Ye,[1] and Yi Cui[1,2,4,*]

SUMMARY

Practical applications of Li-S batteries are hindered by the dissolution/ diffusion loss of sulfur-related active materials in cathode and dendrite growth in Li metal anode. Here we present an integrated sulfur cathode design on tortuosity and sulfur-binding affinity parameters for mitigating diffusion loss of sulfur-based active materials. The high sulfur-philicity property (from oxygen functional groups, 16% in concentration) in reduced graphene oxide (rGO) host favors bonding with sulfur species to mitigate their diffusion/dissolution loss, while the high tortuosity (13.24, from horizontal arrangement of rGO sheets) can localize the soluble active materials within the host rather than outward diffusion loss with subsequent uneven redeposition. With this integrated concept, we achieved ultrahigh cathode areal capacities of 21 mAh cm^{-2} with 98.1% retention after 160 cycles, surpassing those electrodes with lower tortuosity and sulfur-philicity. In addition, same rGO host suppresses dendrite growth in Li anode, enabling 278% prolonged cycle life in the full cell.

INTRODUCTION

The rapid developments of portable electronic devices and electric vehicles have brought about urgent needs for high-energy-density rechargeable batteries.[1–3] The lithium-sulfur (Li-S) battery is widely regarded as one of the most promising energy-storage systems because of its high theoretical energy density (2,567 Wh kg^{-1}) with advantages of environmental abundance, non-toxicity, and low cost of sulfur.[4–7] However, practical applications of Li-S batteries are currently hindered by unsatisfactory cycling stability, which are mainly caused by uncontrolled diffusion of soluble active materials: (1) the lithium polysulfide (LiPS) intermediates, formed during charging and discharging, are highly soluble in commonly used ether-based electrolyte; (2) these soluble LiPS intermediates, originally generated and dissolved in the electrolyte inside the porous cathode, are prone to diffusion outside the cathode and into the electrolyte in the separator, leading to severe active material loss and "shuttle effect;"[8] and (3) during cell charging, large amounts of dissolved LiPS materials that have diffused into the electrolyte outside the cathode are preferentially oxidized to sulfur and redeposited near the top surface of the conductive cathode. This leads to a severe accumulation of sulfur-based species on the top surface of the cathode after repeated cycles,[9] resulting in loss of electric contact, blockage of ion transport into the cathode, increased electrode resistance, deactivated internal active materials, and fast cell failure. Therefore, this diffusion issue of soluble LiPS

Progress and Potential

The high-energy-density Li-S battery is limited by the diffusion loss of active polysulfide (PS) in cathode (degraded cycling capacity/stability) and dendrite growth in Li anode (safety concern). Here, we develop an integrated high-tortuosity and sulfur-philicity design for thick sulfur cathode. The high tortuosity from horizontal alignment of reduced graphene oxide (rGO) sheets, which enhances the physical complexity of mass transport inside the electrode, can localize the soluble PS within the electrode instead of outward diffusion loss. The high sulfur-philicity (from oxygen groups in rGO) favors bonding PS with electrode matrix surface to mitigate its diffusion. With this integrated design, outstanding cathode areal capacities of 21 mAh cm^{-2} and 98.1% retention after 160 cycles are achieved. In addition, the same rGO host suppresses the Li dendrite growth in anode with 278% prolonged cycle life. This high-tortuosity and sulfur-philicity design shows a new principle for future Li-S batteries.

is the important factor that influences the cycling stability of sulfur cathodes, thus impeding the practical applications of high-energy-density Li-S batteries.

To address these problems in sulfur cathode, extensive research has been devoted to decreasing the solubility of LiPS by binding it with solid host materials, such as nanoporous carbon materials to confine sulfur inside the pores,[10] polar surfaces (such as metal oxide) to bind with LiPS,[6] modified binder materials,[11] and new electrolytes with less LiPS solubility.[12] These strategies have focused on mitigating the dissolution of LiPS into electrolyte and have been effective to some extent. However, the diffusion of dissolved LiPS species in the electrolyte can hardly be prevented by these existing LiPS-binding strategies in cathode, and the relationship between LiPS diffusion and electrode structure has received little attention. Under practically high sulfur-loading conditions (>5 mg cm^{-2}) for high-energy-density Li-S batteries,[13,14] dissolution of LiPS materials into electrolyte is inevitable to some extent due to high loading of sulfur active materials, low loading of inactive binding materials, and long cycling requirements. In addition, it was recently discovered that the sulfur cathode material could exist in a supercooled liquid form after being fully charged,[15] suggesting that the liquid-phase diffusion of both LiPS intermediates and sulfur could exist in cathode simultaneously. Due to this uncontrolled diffusion of liquid-form active materials, diffusion loss and redistribution (sulfur accumulation at the top surface of cathode) of active materials are always observed in practical high-loading sulfur cathodes.[9] These issues lead to capacity decay and battery failure. As a consequence, a new electrode design strategy that is capable of addressing both dissolution and diffusion issues simultaneously is important for the realization of practical high-energy-density Li-S batteries.

To find better solutions for these problems, we inspect the relationship between electrode parameters and liquid-phase diffusivity (of LiPS in electrolyte in this case) inside the porous electrode by following Equation b, which is modified from the definition of the MacMullin number (Equation a; N_M, describing the relationship between the real mass diffusivity and intrinsic mass diffusivity of materials, which are dissolved in a liquid electrolyte soaked inside a porous and complex solid electrode):[16,17]

$$N_M = \frac{\tau}{\varepsilon} = \frac{D_{int}}{D_{eff}},$$

(Equation a)

$$D_{eff} = \frac{D_{int} \times \varepsilon}{\tau \times A}.$$

(Equation b)

Here D_{eff} and D_{int} are the effective and intrinsic diffusivities, respectively, of the dissolved LiPS in the liquid electrolyte inside porous electrode. Porosity (ε), tortuosity (τ), and affinity (A, which is also philicity) are three parameters affecting the mass transport inside the porous electrode. Tortuosity is a geometric parameter describing physical complexity of ionic or mass transport inside the porous electrode network.[16] Compared with the definition of the MacMullin number, we further introduce a parameter of affinity/philicity (A) describing the chemical interaction and bonding ability between the porous electrode matrix surface and LiPSs, for mitigation of the diffusion of LiPSs within the porous electrode matrix by their chemical interaction. The higher electrode tortuosity contributes to geometrically extended pathways for LiPS diffusion out from the electrode, while the higher sulfur-philicity represents stronger chemical confinement of LiPS within the electrode.

Based on this theory, here we inspect the relationship between the diffusion-related parameters of the porous host (tortuosity and sulfur-bonding ability), and the

[1]Department of Materials Science and Engineering, Stanford University, Stanford, CA 94305, USA

[2]Stanford Institute for Materials and Energy Sciences, SLAC National Accelerator Laboratory, 2575 Sand Hill Road, Menlo Park, CA 94025, USA

[3]Department of Chemical Engineering, Stanford University, Stanford, CA 94305, USA

[4]Lead Contact

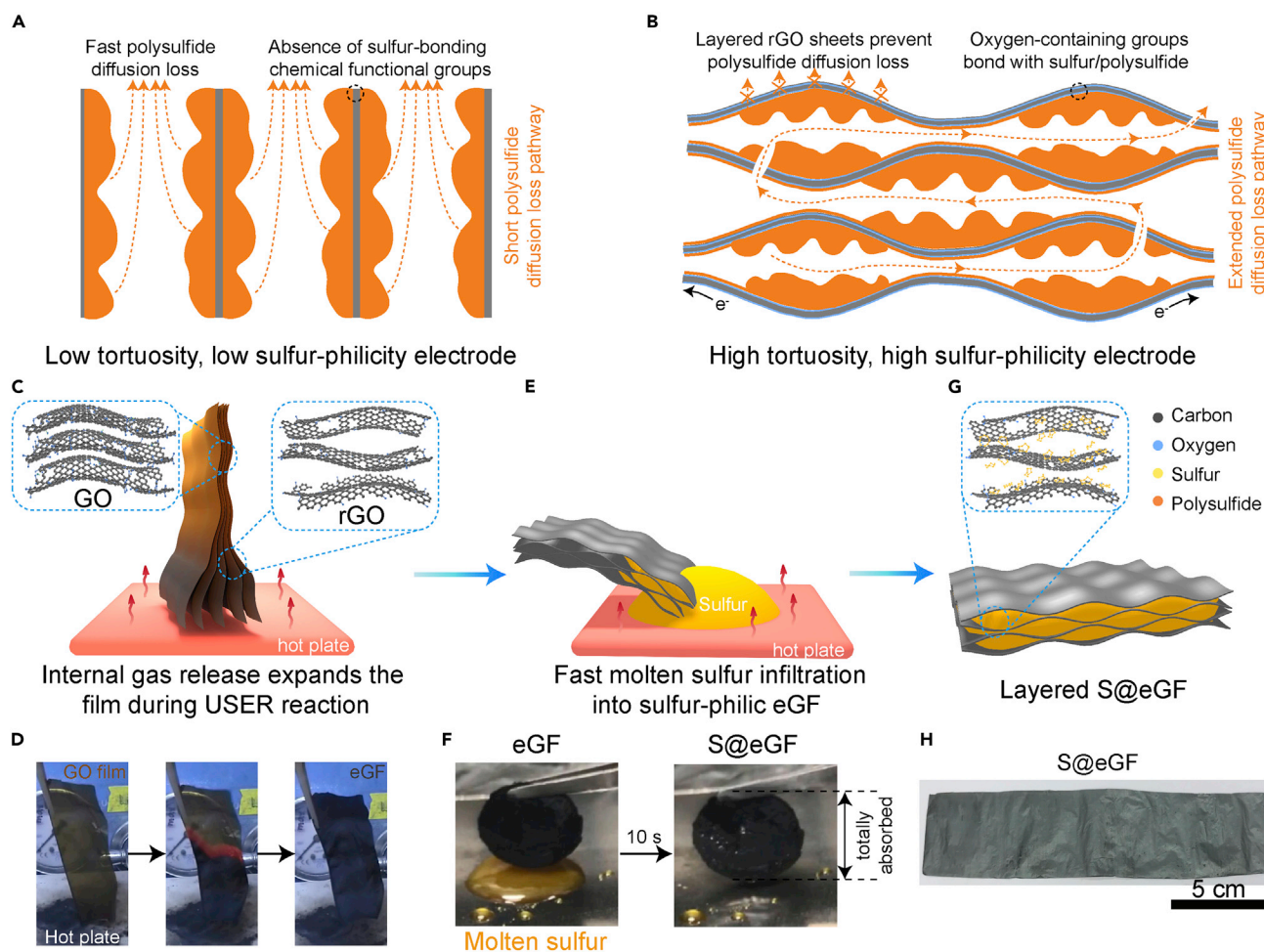*Correspondence yicui@stanford.edu: yicui@stanford.edu

Figure 1. Schematic of Electrode Design and Fabrication

(A) The vertically aligned, low-tortuosity, oxygen-containing functional group-free sulfur@graphene electrode suffers from a severe polysulfide dissolution/diffusion problem due to short LiPS diffusion pathway and absence of sulfur-bonding oxygen functional group.

(B) The horizontally aligned, high-tortuosity, oxygen-containing functional group-abundant sulfur@rGO electrode exhibits less polysulfide dissolution/diffusion loss, owing to significantly extended LiPS diffusion pathway and sulfur-bonding oxygen functional groups.

(C) Schematic of the USER reaction for fabricating eGF electrode.

(D) Digital camera photos of the USER reaction process.

(E) Schematic of the molten sulfur infusion into the nanogaps inside porous eGF when contacted.

(F) Digital camera photos of the fast molten sulfur infiltration process into eGF after 10 s.

(G) Structure illustration of horizontal multi-layered, submicrometer-level sandwiched, sulfur-encapsulated layered S@eGF electrode.

(H) Digital photo of prepared centimeter-scale S@eGF electrode.

electrochemical performances and structure variations of high-loading sulfur cathodes during cycling. For the first time, we reveal that the high tortuosity is a very important electrode parameter for localizing the dissolved LiPS within a porous cathode, which can be further coupled with high sulfur-philicity to achieve an ultrastable and high-loading sulfur cathode. Accordingly, we propose a "high-tortuosity and high-sulfur-philicity" principle for stabilizing high-loading sulfur cathodes, totally different from the traditional low-tortuosity[18] and deep-reduction (oxygen-removing)[19] strategy for conventional Li-ion batteries[20] and low-loading sulfur cathodes.[21,22] These traditional strategies cause severe LiPS dissolution/diffusion loss and redeposition problems that deteriorate cathode performance (Figure 1A). We developed a new ultrafast self-expansion and reduction (USER) reaction to build a

horizontally arranged, high-tortuosity (13.24, representing 1,224% prolonged diffusion pathway) porous reduced graphene oxide (rGO) host electrode with 16% sulfurphilic oxygen concentration. These horizontally arranged rGO sheets extend the mass transport pathway inside the electrode to suppress outward diffusion of LiPS and localize the liquid-phase diffusion of active materials within the porous host, while the oxygen-containing functional groups can bond with sulfur-based species to mitigate LiPS dissolution and diffusion (Figure 1B). This hightortuosity and high-sulfur-philicity sulfur cathode delivers a high areal capacity of 21 mAh cm^{-2} at high sulfur loading of 20 mg cm^{-2}, ~60% capacity at fast charging rate (16 mA cm^{-2}), and 98.1% capacity retention with stable cathode structure and resistance after 160 cycles. In comparison, the low-tortuosity (4.91) and low-sulfurphilicity (0.5% oxygen concentration) electrodes exhibit obvious electrode structure change (LiPS dissolution/diffusion loss and redeposition) and ~33% capacity loss after only 75 and 5 cycles, respectively, revealing the strong correlation between tortuosity and sulfur-philicity parameters and cathode performances. Additionally, the same rGO host can also resolve the Li dendrite growth issue on the anode side, helping prevent dangerous short-circuiting and extending battery cycle life by 278%.

RESULTS AND DISCUSSION

The high-tortuosity, high-sulfur-philicity electrode was fabricated through a facile USER reaction, followed by molten sulfur uptake as summarized schematically in Figures 1C–1H. The starting material of free-standing and densely stacked graphene oxide film (GoF) was fabricated on a decimeter scale by blade coating an aqueous graphene oxide (GO) solution onto a glass substrate, followed by peeling off after drying (Figure S1). When the GoF was partially put into contact with a 350°C hotplate inside an argon-filled glovebox, the USER reaction happened immediately from the touchpoint and quickly spread across the whole film within milliseconds (Figures 1C and 1D; Video S1), exhibiting color change from semi-transparent brown to nontransparent black, expansion in thickness, and gas release from inside of the film. This USER reaction occurs due to the fast decomposition and removal of abundant oxygen-containing functional groups in GO when superheated[23] (36% loss in weight, Figure S2A), which is *in situ* cracked into carbon monoxide and dioxide gases and generates internal pressure within rGO layers (Figures S2B and S2C), similar to the thermal-triggered decarboxylation reaction. The generated gases and internal pressure were immediately released to create nanogaps between horizontal rGO layers, achieving the expanded reduced graphene oxide film (eGF) with high tortuosity from horizontal rGO sheets. With a high ΔH of approximately 1680 J g^{-1} that corresponds to an estimated adiabatic final temperature of 1,240°C,[24] this exothermic USER reaction can rapidly heat up the nearby GO sheets to initiate further USER reaction (starting temperature of around 150°C), thus spreading through the while GO film. Meanwhile, a modest amount of oxygen-containing groups remained in the rGO layers, enabling high sulfur-philicity for molten sulfur infusion and bonding.[25] After this USER reaction, sulfur was rapidly and homogeneously absorbed into the nanogaps by simply bringing the edge of eGF into contact with molten sulfur (160°C, within 10 s) (Figures 1E and 1F; Video S2), which is believed to be due to the synergetic effects of sulfur-philic nature of eGF and the capillary force produced by the submicrometer-scale channels. Compared with conventional electrode fabrication approaches such as liquid-phase synthesis or slurry coating, this USER reaction with thermal infusion method has several distinguishing advantages: (1) no use of toxic organic solvents (methylpyrrolidone for making slurry or carbon disulfide for creating sulfur composites) or binders is needed; (2) high sulfur weight ratio (80 wt % in this case, Figure S3) and sulfur loading can be easily

controlled with good uniformity in the electrode (Figures 1G and 1H); and (3) facile fabrication steps and abundant raw materials enable decimeter-scale electrode fabrication (Figure 1H). These merits confer great significance for large-scale manufacturing and real battery applications.

In addition to the high-tortuosity and high-sulfur-philicity S@eGF electrode, we also designed low-tortuosity and low-sulfur-philicity electrodes for comparison. Utilizing an ice-templated unidirectional freeze-drying method[26] followed by USER reaction, we fabricated expanded vertically aligned rGO aerogel (eVGA) (Figure S4) that possesses the same chemical composition as eGF yet with lower electrode tortuosity (because of the vertical alignment of rGO sheets and channels). Another control electrode with low tortuosity and low sulfur-philicity was created using a thermal-shock reaction to totally remove the oxygen-containing functional groups in eVGA at 3,000 K,[27] designated as low-tortuosity and low-sulfur-philicity eVGA-3k electrode. A molten sulfur droplet was rapidly absorbed into the high-sulfur-philicity eVGA host to achieve S@eVGA cathode (within 13 s) (Figure S5A and Video S3), but very slowly infiltrated into eVGA-3k to fabricate S@eVGA-3k electrode (within 60 s) (Figure S5B and Video S4). The slow infiltration of sulfur into eVGA-3k is due to its deep degree of reduction and low oxygen concentration, which yield low sulfur-philicity. This illustrates that the sulfur-philicity has distinct advantages for uniform sulfur absorption into electrodes (Figure S5C), which should also benefit electrode fabrication and performance.

The differences in electrode alignments and tortuosities were first investigated by scanning electron microscopy (SEM). After the USER reaction, the original 30-μm-thick, continuously and densely stacked layered structure of GO film (Figure S6) turned into the porous layered structure of eGF with an obvious thickness increase to around 90 μm (Figure 2A). Most rGO sheets in eGF were horizontally arranged to extend the mass transport pathway inside the electrode, resulting in high electrode tortuosity. The magnified SEM images of eGF exhibited abundant horizontal capillary void channels (diameters of several hundred nanometers) between horizontally arranged rGO sheets (inset in Figure 2A), which is due to the internal gas release during the USER reaction. These submicrometer-scale channels not only enable capillary forces for sulfur absorption into the porous host but also provide predefined space for sulfur intake and storage. After molten sulfur infusion, sulfur particles were uniformly confined in the channels between horizontal rGO sheets as designed (Figures 2B and S7A). Energy-dispersive X-ray spectroscopy (EDX) mapping on a cross-section of the S@eGF electrode also demonstrates the uniform distribution of carbon, oxygen, and sulfur species across the thickness of electrode (Figure 2C). Magnified cross-sectional SEM images of S@eGF exhibited a uniform periodic stacking of submicrometer-scale sandwich structures, with well-encapsulated sulfur particles between the horizontal rGO sheets (Figure 2D). This homogeneous, horizontal multi-layered submicrometer-level sandwich structure enables better electronic contact and utilization of active materials, while the abundant horizontal rGO sheets extend the outward diffusion pathway to mitigate the loss of active materials via the high-tortuosity design (Figure 1B). In addition, several vertical channels and void spaces also exist inside the electrode for inward electrolyte infiltration and lithium ion transport (Figures S7C and S7D). These results demonstrate the uniform and high-loading sulfur storage inside this horizontally arranged rGO host, which is consistent with the high-tortuosity and sulfur-philic design.

In comparison with the horizontally arranged, high-tortuosity S@eGF electrode, the S@eVGA and S@eVGA-3k electrodes exhibit vertically aligned structures with lower
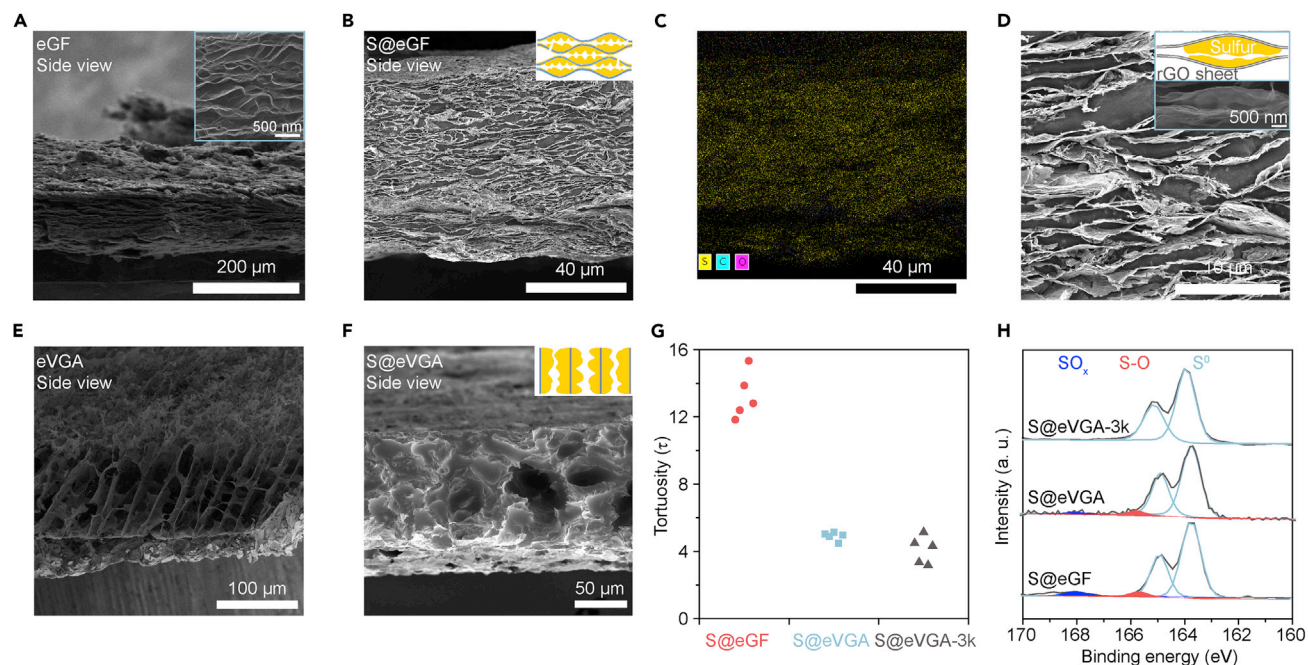
Figure 2. Characterizations of Different Electrodes

(A) Cross-sectional SEM images of eGF. Inset shows the magnified SEM image on the cross-section of eGF.

(B and C) Cross-sectional SEM image of S@eGF (B) with corresponding element distribution mapping (C). Inset shows schematic illustrating the sulfur particles encapsulated by horizontal rGO sheets structure.

(D) Magnified cross-sectional SEM images of S@eGF showing the clear horizontal multi-layered, submicrometer-level sandwiched structure of sulfur particles encapsulated by horizontal rGO sheets. Inset shows the further magnified SEM image and schematic of this sandwiched structure of S@eGF.

(E) Cross-sectional SEM image of eVGA.

(F) Cross-sectional SEM image of S@eVGA. Inset shows schematic illustrating the sulfur particles encapsulated between vertical rGO sheet structure.

(G) Tortuosity measurement of different sulfur-containing electrodes.

(H) S_{2p} XPS spectra of different sulfur cathode. $x = 2–4$.

electrode tortuosity. Owing to the perpendicularly grown ice template, the rGO sheets and channels inside eVGA were all vertically aligned throughout the electrode (Figures 2E and S8). Meanwhile, submicrometer-sized channels also existed in the vertical rGO walls due to the gas pressure release during the USER reaction (Figure S8F), which also contributes to the capillary force for sulfur infusion into the electrode. After the 3,000 K thermal-shock reaction, the vertically aligned host with channeled structure still remained in the eVGA-3k (Figure S8G). These vertical channeled structures of eVGA and eVGA-3k differ from the horizontally arranged structure of eGF, leading to significant differences in electrode tortuosities. After the molten sulfur infiltration into eVGA or eVGA-3k, the sulfur particles were uniformly absorbed onto the vertical rGO walls and stored inside the vertical channels of the hosts (Figure 2F), exhibiting a short vertical outward path for active material diffusion (Figures S9 and S10) that is consistent with the common low-tortuosity electrode design.

The differences in electrode tortuosities were directly measured by a blocking electrolyte impedance method developed by the Gasteiger group.[28] By measuring the ionic resistance in a symmetric cell using a non-reactive blocking electrolyte (Figure S11), the average tortuosity of S@eGF is determined to be around 13.24 (Figure 2D), suggesting that the average length of mass transportation pathway out of this 80-μm-thick S@eGF is around 1,059 μm. In comparison, S@eVGA and S@eVGA-3k electrodes exhibit much lower tortuosity of around 4.91 and 4.09,

respectively. This higher tortuosity of eGF over eVGA is also supported by a polarization-interruption measurement,[16] exhibiting slower mass transportation speed inside the eGF than in the eVGA electrode (Figure S12). These characterizations demonstrate that the different alignment direction of rGO sheets and channels inside the host leads to different electrode tortuosity and length of mass transport pathway, which should have significant impact on diffusion of dissolved LiPS, electrochemical performance, and stability. In addition, eGF and eVGA show very similar Brunauer-Emmett-Teller surface area (both around 210 $m^2 g^{-1}$, Figure S12C) and pore size distribution (Figure S12D), suggesting no difference in sulfur and polysulfide confinement by the micropores and mesopores in the rGO sheets inside eGF and eVGA electrodes.

In addition to the different alignment directions and tortuosities, the S@eGF and S@eVGA electrodes exhibited similar oxygen-containing composition to enable their sulfur-philicity that differs from that of the S@eVGA-3k electrode. The X-ray photoelectron spectroscopy (XPS) spectra of eGF and eVGA exhibit similar moderate oxygen concentration of ~16% with high intensity C–O/C=O bonding peaks in C_{1s} and O_{1s} spectra, while eVGA-3k shows a negligible amount of oxygen concentration as low as 0.5% (Figure S13). This proves that the difference between eVGA and eVGA-3k lies in the concentration of oxygen-containing groups caused by different degrees of reduction, which is also supported by the significantly increased crystallinity in X-ray diffraction (XRD) spectra (Figure S14) and decreased intensity of D band in Raman spectra of eVGA-3k (Figure S15). Importantly, the S_{2p} XPS spectra of S@eGF and S@eVGA exhibit clear sulfur-oxygen bonding peaks at 166 eV and 168 eV, while the S@eVGA-3k exhibits total absence of these peaks (Figure 2H). This S_{2p} XPS spectrum demonstrates that the oxygen-containing groups in eVGA and eGF can bond with sulfur species to improve electrode sulfur affinity/-philicity.[6,25,29] This is consistent with the aforementioned significantly enhanced sulfur absorption speed of eGF and eVGA over that of eVGA-3k, which should also have a positive impact on mitigating LiPS dissolution/diffusion loss and improving electrochemical performance.

The influences of tortuosity and sulfur-philicity properties on electrochemical performances were first investigated by galvanostatic cycling of different sulfur cathodes (Figure 3A) using excess Li metal as the counter electrode. With high sulfur loading of 10 mg cm^{-2} in the cathode and relatively low electrolyte amount of 7 $\mu L\ mg_{sulfur}^{-1}$, the high-tortuosity and high-sulfur-philicity S@eGF cathode exhibited high specific capacity of 1,084, 877, 686, and 561 mAh g^{-1} at current densities of 1.6, 3.2, 8, and 16 mA cm^{-2}, respectively. The voltage profiles of S@eGF cathode show typical two-plateau charge/discharge curves with low overpotentials (190 and 285 mV at current densities of 1.6 and 8 mA cm^{-2}, respectively; Figure S16A), suggesting the kinetically efficient electrochemical reaction process with small barriers even under such a high sulfur loading and lean electrolyte condition. Impressively, the S@eGF cathode showed 98.1% capacity retention and nearly overlapping charge/discharge curves after 160 cycles (Figure 3B), with high Coulombic efficiency of over 97%. The shortening and voltage drop of first discharge plateau at the 150th cycle are due to the accumulated solid electrolyte interphase (SEI) in Li metal anode after repeated Li stripping/plating cycling, which will increase the overall overpotential and resistance of the battery especially at the relatively early stages of battery discharging and Li stripping.[30,31] Additionally, electrochemical impedance spectroscopy (EIS) exhibits low and stable cathode charge-transfer resistance (middle frequency semicircle)[32] of ~3.5 Ω even after 150 cycles (Figure 3C). These high and stable capacities illustrate the excellent suppression of LiPS dissolution and
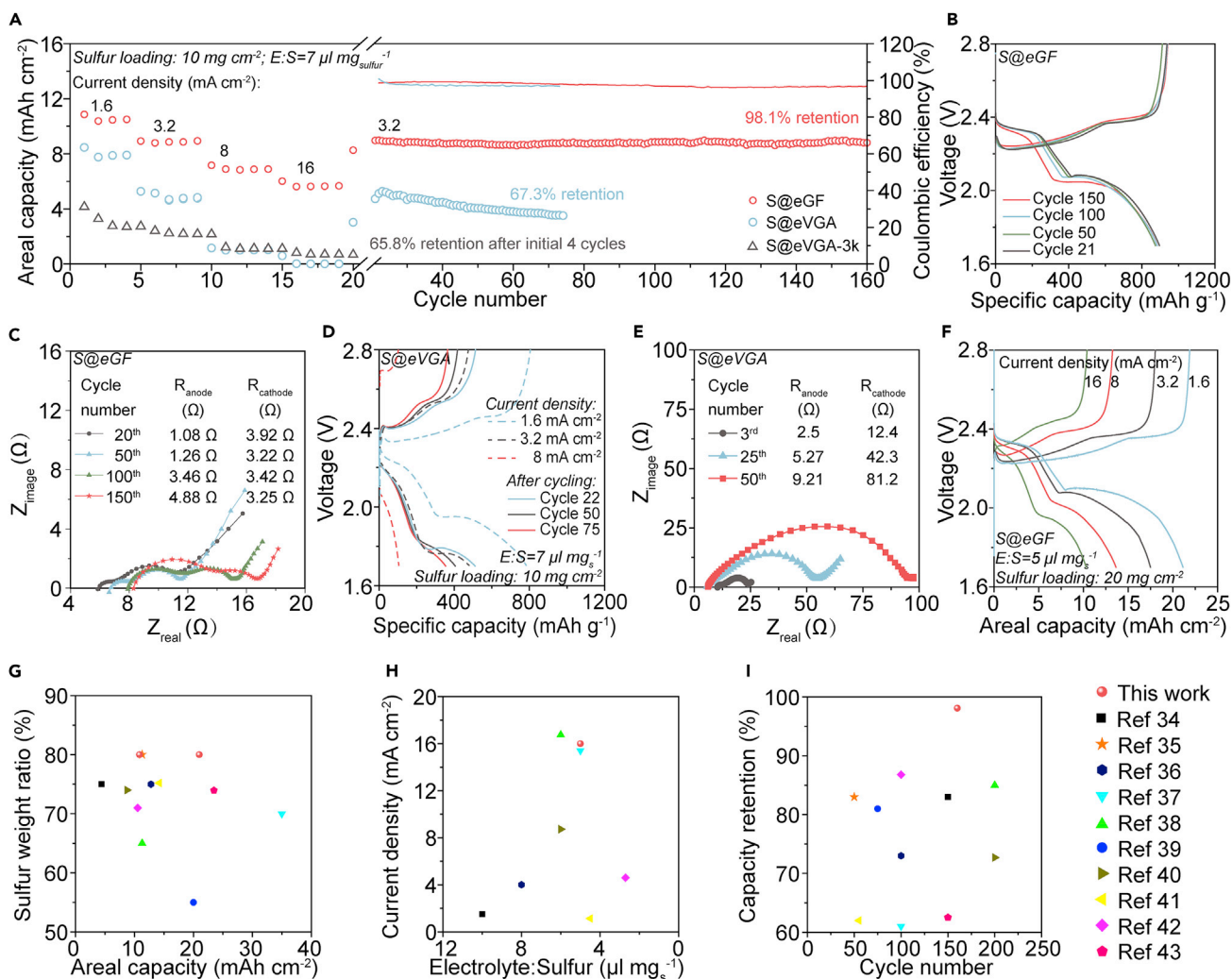
Figure 3. Electrochemical Performances of the Different Sulfur Cathodes

(A) Rate capabilities and cycling performances of different cathodes with sulfur loading at 10 mg cm^{-2}. E:S, electrolyte:sulfur ratio.

(B) Voltage-capacity plot of S@eGF cathode after different cycles with sulfur loading at 10 mg cm^{-2}.

(C) EIS spectra of S@eGF cathode after different cycles with sulfur loading at 10 mg cm^{-2}. Inset shows the fitting results.

(D) Voltage-capacity plot of S@eVGA cathode at different current densities and after different cycles with sulfur loading at 10 mg cm^{-2}.

(E) EIS spectra of S@eVGA cathode after different cycles with sulfur loading at 10 mg cm^{-2}. Inset shows the fitting results.

(F) Voltage-capacity plot of S@eGF cathode at different current densities with sulfur loading at 20 mg cm^{-2}.

(G–I) Comparisons of electrode parameters and performances between this work and recently published literatures, in terms of areal capacity with sulfur weight ratio (G), electrolyte:sulfur ratio with highest current density (H), and cycle number with capacity retention (I).

diffusion-induced active material loss and electrode passivation in the S@eGF cathode, which can be attributed to the high electrode tortuosity and sulfur-philic design.

In comparison, the low-tortuosity S@eVGA and low-sulfur-philicity S@eVGA-3k electrodes exhibited degraded performances compared with S@eGF, despite having the same sulfur loading, weight ratio, and carbonaceous host. The high-sulfur-philicity yet low-tortuosity S@eVGA cathode afforded lower capacity of 775, 472, and 100 mAh g^{-1} at current densities of 1.6, 3.2, and 8 mA cm^{-2}, respectively, along with significantly increased overpotential of 452 and 740 mV at current density of 1.6 and 8 mA cm^{-2}, respectively (Figure 3D). After 75 cycles, only 67.3% of original

capacity was retained, with clear voltage drop of the second discharge plateau. The EIS spectrum also illustrates large increases in cathodic charge-transfer resistance (middle frequency semicircle) from 12.4 to 81.2 Ω after only 50 cycles (Figure 3E). Compared with the high-tortuosity and kinetically stable S@eGF, these deteriorated electrode kinetics and capacity in S@eVGA should be attributed to increased LiPS diffusion through the low-tortuosity host, which leads to severe active material loss and electrode passivation.[4] Moreover, the low-tortuosity and less sulfur-philic S@eVGA-3k electrode showed much lower capacity of 409, 233, and 152 mAh g^{-1} at current densities of 1.6, 3.2, and 8 mA cm^{-2}, respectively, along with fast capacity decay (34.2% loss, Figure 3D) and severe electrode passivation (cathodic resistance increase from 11.1 to 150 Ω, Figure S17) after only five cycles. These comparisons prove that the deteriorated electrochemical performances of increased polarization, sluggish redox reaction kinetics, and fast capacity fading are strongly correlated with the electrode tortuosity and sulfur-philicity parameters, which are critically important for the stable performance of a high-loading sulfur cathode.

Benefiting from the effective high-tortuosity and sulfur-philicity design, the active material loading in S@eGF cathode was further enhanced without degrading its electrochemical performance. With low electrolyte amount of 5–7 μL mg$_{sulfur}$$^{-1}$, the S@eGF cathodes exhibited high areal capacities of 13.7, 15, and 21 mAh cm^{-2} when the sulfur loadings were further enhanced to 12, 15, and 20 mg cm^{-2}, respectively (at current density of 1.6 mA cm^{-2}, Figure S18), along with high capacities (6.3, 7.5, and 12 mAh cm^{-2}, respectively) and clear two-plateau charge/discharge curves even at high current density of 16 mA cm^{-2} (Figures 3F and S18). Good electrode reversibility was also achieved in these ultrahigh-loading S@eGF cathodes, exhibiting 92.2%–94.5% capacity retention, stable and low-overpotential voltage profiles, and high Coulombic efficiency of >98% even after 110 cycles (for sulfur loading at 12 and 15 mg cm^{-2}) and 70 cycles, respectively (for sulfur loading at 20 mg cm^{-2}, Figure S18). Compared with other high-loading sulfur cathodes in recently published literature, this S@eGF cathode achieved one of the best performances and key technical parameters (Figures 3G–3I),[33–43] which should be attributed to the effective high-tortuosity and sulfur-philicity design.

To elucidate how the high tortuosity and sulfur-philicity contribute to the stable electrochemical performance, we inspected the morphology variations of different cathodes after cycling. As shown in the cross-sectional SEM image of a cycled S@eGF cathode (Figure 4A), the original horizontal multi-layered, submicrometer-level sandwiched electrode structure was well maintained even after 160 cycles, exhibiting uniformly distributed sulfur species across the thickness of the electrode. Further magnified SEM images of cycled S@eGF show that the sulfur particles were still confined between horizontal rGO layers (Figure 4B), and top-view SEM images show the absence of a redeposited sulfur particle on the surface of electrode (Figures S19A–S19C). This good morphological consistency between cycled and fresh S@eGF electrodes demonstrates successful suppression of soluble LiPS diffusion and active material loss. In comparison, the cross-sectional and top-view SEM images of low-tortuosity S@eVGA electrode exhibited an obvious morphology change after cycling: a 5-μm-thick sulfur layer was observed lying above the vertical rGO sheets (Figures 4C and S19D), which is totally different from the uniform vertical channeled structure of S@eVGA before cycling (Figure 2F). This accumulated surface layer on the top surface of the electrode was created by the diffusion and redeposition products of soluble sulfur-based active materials,[9] which were originally stored in the vertical channels between vertical rGO sheets. Such an accumulated surface sulfur layer loses electronic contact with the current collector and becomes "dead sulfur" and blocks inward ion transportation to passivate and render the internal
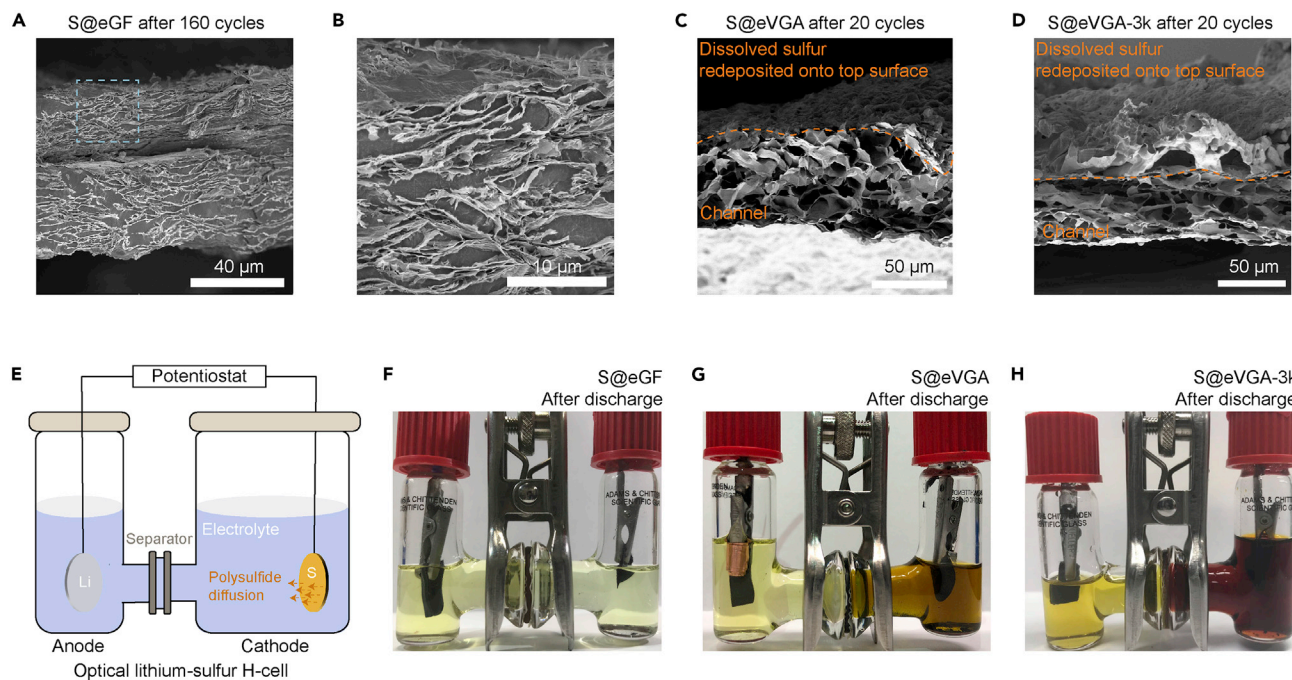
Figure 4. Morphology Variation and LiPS Dissolution/Diffusion Loss Evaluation of Different Cathodes after Cycling

(A and B) Cross-sectional SEM images of S@eGF after 100 cycles (A). Magnification of the square region in (A) is shown in (B).

(C) Cross-sectional SEM image of S@eVGA after 20 cycles.

(D) Cross-sectional SEM image of S@eVGA-3k after 20 cycles. The orange dashed lines show the boundaries between redeposited sulfur species accumulated on top surface and original vertical rGO matrix of electrode.

(E) Schematic of H cell for evaluation of LiPS diffusion loss.

(F–H) Digital photos of H cells with different cathodes (S@eGF [F], S@eVGA [G], S@eVGA-3k [H]) after single discharge step. The color change of electrolyte inside cathode-side H-cell compartment represents the severity of LiPS outward diffusion loss from different tortuosity cathodes.

sulfur electrode less electrochemically accessible.[9] This failure mechanism is consistent with the previous capacity fade and deteriorating kinetics phenomenon in the S@eVGA electrode. Moreover, the low-sulfur-philicity S@eVGA-3k electrode exhibited a more severe phenomenon of uneven LiPS diffusion/redeposition. Large amounts of sulfur species were dissolved out, redeposited, and turned into a 16-μm-thick sulfur layer on the top surface of the electrode (Figure 4D). These sulfur/LiPS diffusion and redeposition issues were commonly regarded as the key cause of capacity and kinetic degradation problems in conventional high-loading sulfur electrodes.[9] These comparisons between morphology variations in electrodes of different tortuosity and sulfur-philicity directly reveal that the low-tortuosity and sulfur-philicity parameters lead to more severe LiPS dissolution/diffusion loss and redeposition problems during cycling of a high-loading sulfur cathode, resulting in active material loss and invalidation of internal electrode active material that is strongly correlated with deterioration of battery performance.

The severity of LiPS diffusion loss in electrodes of different tortuosity and sulfur-philicity was directly visualized in a transparent H cell (Figure 4E). The sulfur cathode and lithium anode were inserted into the electrolyte-filled H cell inside an argon-filled glovebox and connected to a potentiostat. During the galvanostatic discharge, LiPSs were gradually dissolved and diffused out from the cathode into the electrolyte with obvious color change, which qualitatively confirms the severity of LiPS dissolution/diffusion. After a single discharge step, the S@eGF cathode exhibited a tiny amount of diffused LiPS with negligible color change in the electrolyte
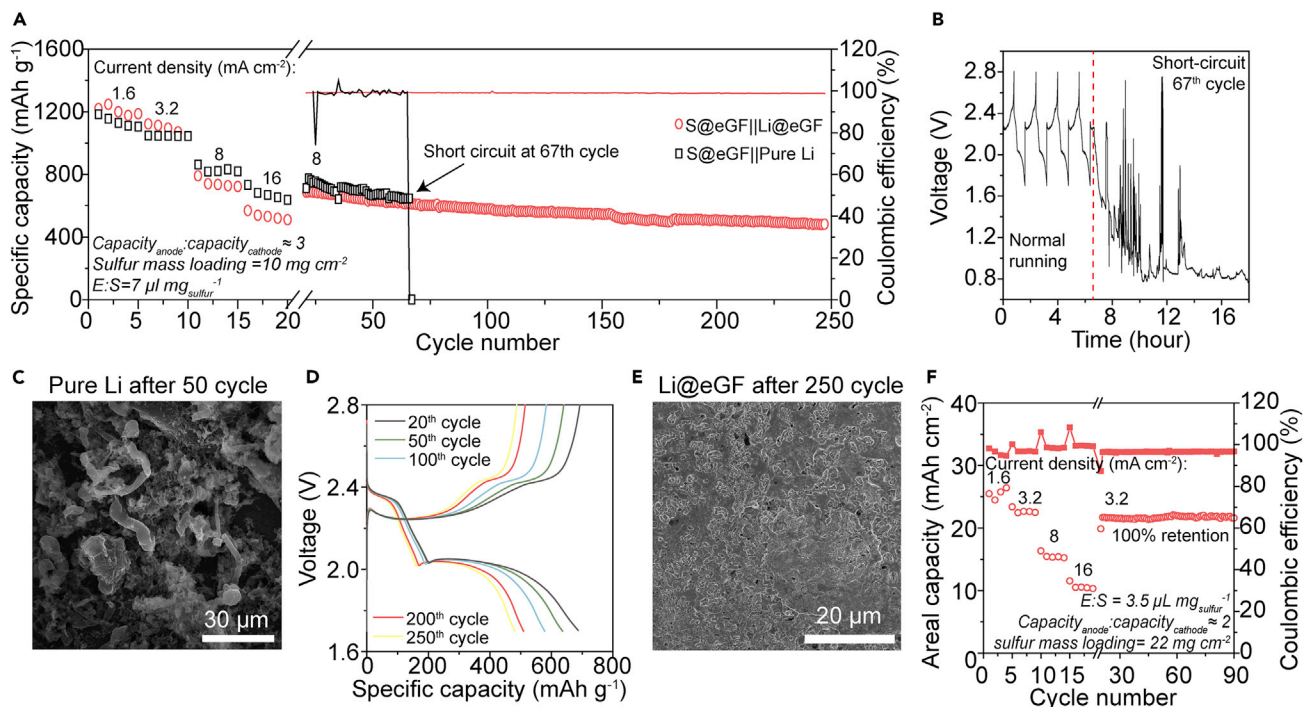
Figure 5. Full-Cell Performances with Both Hosted Anode and Cathode

(A) Lithium-sulfur full-cell cycling performances using S@eGF cathode and different anodes of pure lithium metal (black) or Li@eGF (red).

(B) Voltage-time plot of S@eGF||pure Li cell at the short-circuit 67th cycle.

(C) Top-view SEM image of pure Li metal anode after 50 cycles.

(D) Voltage-capacity plot of S@eGF||Li@eGF cell after different cycles.

(E) Top-view SEM image of Li@eGF anode after 250 cycles.

(F) Cycling performance of S@eGF||Li@eGF full cell using S@eGF cathode (sulfur mass loading of 22 mg cm^{-2}) with low E:S ratio (3.5 μL mg^{-1}) and limited amount of Li@eGF anode (13 mg cm^{-2}, ~50 mAh cm^{-2}).

(Figure 4F). In comparison, the S@eVGA exhibited gradually slow color change of electrolyte during discharging (Figure S20), and finally a semi-transparent orange electrolyte after a single discharge step due to moderate diffusion amount of dissolved LiPS. Moreover, the S@eVGA-3k showed severe diffusion of dissolved LiPS from the electrode, which turned the original transparent colorless electrolyte into a brownish-red opaque electrolyte. These H-cell data are consistent with the Li-S battery cycling data using ether electrolyte without LiNO$_3$ additive, showing that the S@eGF cathode retained 85.2% capacity with relatively lower yet stable Coulombic efficiency (93.7%) after 100 cycles, while the S@eVGA cathode exhibited a severe shuttle effect and failure to be fully charged at the 23rd cycle (Figures S20D and S20E). These comparisons between different H cells and cycling performances demonstrate that both high electrode tortuosity and high sulfur-philicity significantly contribute to the suppression of LiPS diffusion, which should both be important for improving the electrochemical performances of high-loading sulfur cathodes (Figure S20F).

In addition to the decent electrochemical performance achieved in the cathode, this high-loading Li-S battery faces another critical short-circuit problem arising from the lithium metal anode side that limits cycle life and safety of the battery. As shown in Figure 5A, the S@eGF||pure Li full cell using a conventional pure Li metal foil anode exhibited a severe cell short-circuit after only 66 cycles at a higher current density of

8 mA cm^{-2}, showing a fast voltage drop from 2.2 V to lower than 1.2 V and failure to be charged back to normal working voltage range (Figure 5B). A SEM image shows that large amounts of wire-shaped Li dendrites existed on the top surface of cycled Li metal anode (Figure 5C), which was extracted from the S@eGF||pure Li full cell after 50 cycles. These dendrites can easily pierce the separator to cause a battery short-circuit, leading to severe compromise to cell-cycle life and safety. To solve this problem, we also fabricated a hosted lithium metal anode (Li@eGF) by molten lithium infusion into eGF (Video S5), which can mitigate the infinite volume change of Li metal anode and decrease local current density to suppress dendritic growth.[44] Using this hosted Li@eGF anode (~7.5 mg cm^{-2}, ~30 mAh cm^{-2}), the S@eGF||Li@eGF full cell exhibited significantly prolonged cycle life of up to 250 cycles (Figure 5A), along with relatively stable and clear two-plateau charge/discharge curves during cycling (Figure 5D). Top-view SEM images of Li@eGF electrode after 250 cycles (Figures 5E and S21) show a relatively flat surface absent of wire-shaped dendrites, illustrating that this prolonged cycle life and avoidance of cell failure are due to the successful suppression of dendrite growth by the eGF host. With further enhanced mass loading in cathode (22 mg cm^{-2}), lower electrolyte amount (electrolyte/sulfur ratio of 3.5 μL mg$_{sulfur}^{-1}$), and lean anode amount (13 mg cm^{-2}), the S@eGF||Li@eGF full cell exhibits an ultrahigh areal capacity of 25 mAh cm^{-2} and 100% capacity retention after 90 cycles with stable charge/discharge curves (Figure 5F), achieving an estimated energy density as high as 395 Wh kg^{-1} (Figure S22). These data reveal that this eGF host successfully improves the electrochemical performance of not only sulfur cathodes but also lithium metal anodes, which holds great significance for future high-energy-density Li-S batteries.

Conclusions

We propose a "high-tortuosity and high-sulfur-philicity" principle whereby high electrode tortuosity and high oxygen concentration are the key parameters for controlling the diffusion behaviors of soluble active materials inside the cathode, which is important for improving the electrochemical performances and cycling stabilities of ultrahigh-loading sulfur cathodes. The horizontally arranged rGO sheets in high-tortuosity eGF (13.24) extend the outward diffusion pathway of active materials to localize the dissolved LiPS within the porous cathode, while the oxygen functional groups in rGO sheets (16% in concentration) can bond with sulfur species to mitigate LiPS dissolution/diffusion loss. Benefiting from these high-tortuosity and high-sulfur-philicity properties, a high areal capacity of 21 mAh cm^{-2}, ~60% capacity retention at fast charging rate (16 mA cm^{-2}), and 98.1% retention with stable cathodic resistance after 160 cycles were realized in this ultrahigh sulfur-loading S@eGF cathode, far surpassing those of low-tortuosity (4.91), low-oxygen-concentration (0.5%) counterparts. SEM characterizations of cycled electrodes and *in situ* optical H cells demonstrated that the severity of LiPS diffusion and dissolution is positively correlated with the decreased tortuosity and oxygen concentration, respectively, leading to undesired dead sulfur deposition onto the top surface of cathode, invalidation of internal active materials, and deteriorated kinetics. Additionally, this porous eGF host also effectively suppresses the dendrite growth in lithium metal anodes, contributing to 278% extension in battery cycle life and prevention of dangerous dendrite-induced cell short-circuiting. By addressing the electrochemical performances and stability issues of both electrodes simultaneously, our large-scale manufacturable eGF electrode not only provides a promising design principle for electrodes suffering from liquid-phase diffusion loss issues, but also paves the way for next-generation high-energy-density Li-S batteries with long cycle life and safe operation.

EXPERIMENTAL PROCEDURES

Resource Availability

Lead Contact

Further information and requests for resources and reagents should be directed to and will be fulfilled by the Lead Contact, Yi Cui (ycui@stanford.edu).

Materials Availability

This study did not generate new unique reagents.

Data and Code Availability

This study did not generate/analyze [datasets/code].

Preparation of eGF

Commercially available GO solution (Hangzhou Gaoxi Technology, 9 mg mL^{-1}) was blade coated onto glass substrate using a doctor blade and dried at room temperature. The dried GoF was peeled off from the glass substrate and transferred into an argon-filled glovebox. The USER reaction was conducted by connecting one side of GoF to the 350°C hotplate inside the glovebox (Video S1). The GoF was quickly reduced and self-expanded into eGF, together with color change from light orange to black and obvious gas release from inside.

Fabrication of eVGA and eVGA-3k

GO solution was filled into a polyimide O-ring mold and transferred onto a cold plate. Liquid nitrogen was injected into the cold plate below the mold to achieve vertical unidirectional freezing of GO solution. The frozen GO-ice solution was dried under vacuum for 24 h to fabricate the vertical GO aerogel, followed by USER reaction to fabricate eVGA inside the glovebox. By a thermal-shock reaction, eVGA can be annealed at 3,000 K to totally remove oxygen-containing groups and restore graphene structure into eVGA-3k.[27]

Preparation of S@eGF, S@eVGA, and S@eVGA-3k Cathodes

A controlled amount of sulfur (10 mg) was placed onto a hotplate and annealed to 155°C to obtain a molten sulfur droplet inside an argon-filled glovebox. The sulfur-containing cathode was prepared by bringing the edge of rGO host (eGF, eVGA, and eVGA-3k) into contact with the sulfur droplet until completely absorbing sulfur into the host, as shown in Videos S2, S3, and S4.

Tortuosity Measurements

For the blocking electrolyte impedance method, symmetrical cells were fabricated using S@eGF (or S@eVGA, S@eVGA-3k) as both electrodes, glass fiber as separator, and 50 mM tetrabutylammonium perchlorate in ethyl carbonate/dimethyl carbonate (1:1 [v/v], ionic conductivity of 1.74 mS cm^{-1}) as blocking electrolyte. The EIS spectrum was recorded with a VMP3 potentiostat (BioLogic) from 200 kHz to 50 mHz with an AC voltage amplitude of 10 mV at the open-circuit potential, which was repeated using several samples and several times for accuracy. The ionic resistances were extracted from the EIS spectra to calculate electrode tortuosity.[17,28] The detailed calculation steps are shown in Figure S11.

For the polarization-interruption mode, the eGF-embedded (or eVGA) polyimide O-ring was placed between two Celgard 2325 separator coated lithium metals, soaked by electrolyte, and assembled into cells.[16,17] The assembled cells were tested using a battery tester. A stable SEI on the lithium metal was formed by cycling consisting of passing a constant current (0.5 mA cm^{-2}) for 10 min, followed by a 3-min rest period,

then passing current in the reverse direction under the same conditions. After the conditioning cycles, a constant current of 2 mA cm^{-2} was applied for 2 min to set up a concentration gradient in the cell. The concentration gradient was then allowed to relax by interrupting the current until the cell potential approached zero. Thereafter the current direction was reversed for 2 min followed by interruption of the current until the cell potential approached zero. The relaxation of the concentration gradient was observed in terms of a cell-potential decay with time. The thickness of the polyimide O-ring was the same as that of eGF and eVGA electrodes to keep their aligned structure from being damaged.

Fabrication of Li@eGF Anode

Solid lithium was annealed to 350°C on a hotplate to obtain a molten lithium droplet inside an argon-filled glovebox. The lithium-containing Li@eGF anode was prepared by contacting eGF with the molten lithium droplet to absorb lithium into the host, as shown in Video S5.

Electrochemistry

Battery cycling performance was evaluated by the galvanostatic cycling of coin cells (CR-2032) with S@eGF, S@eVGA, or S@eVGA-3k cathode assembled in an argon-filled glovebox, with lithium metal (Hydro-Québec) or Li@eGF as counter electrodes, and one layer of Celgard separators (Celgard 2325, 25 μm thick) was used to separate the electrodes. The electrolyte was prepared by dissolving an appropriate amount of lithium bis(trifluoromethanesulfonyl)imide (1 M) in 1:1 (v/v) dimethoxyethane ether (DME) and dioxolane containing LiNO$_3$ (0.25 M). A controlled amount of electrolyte (3.5–7 μL mg$_{sulfur}$$^{-1}$, based on different areal loadings) was added onto cathode and separator during cell assembly. Battery cycling data were collected using a Landt or Arbin eight-channel battery tester at room temperature with voltage range of 1.7–2.8 V. The current densities were varied between 1.6 and 16 mA cm^{-2}, and calculated specific capacities were based on the mass of sulfur in the cathode. EIS data were obtained with a VMP3 potentiostat (BioLogic) from 200 kHz to 50 mHz with an AC voltage amplitude of 10 mV at the open-circuit potential.

The LiPS diffusion test was conducted in a gas-tight, two-compartment optical H cell with compartments separated by one piece of Celgard 2325 separator (Figure 4E). S@eGF cathode (or S@eVGA and S@eVGA-3k, area of 1 cm^{-2}) and lithium foil were clamped to current collectors and inserted into a sealed H cell. Five milliliters of electrolyte was injected into the H cell. The optical H cell was stored inside an argon-filled glovebox and connected to a VMP3 potentiostat (BioLogic) and discharged at current density of 0.2 mA to 1.7 V. The change of electrolyte color qualitatively determined the severity of LiPS dissolution/diffusion loss of different cathode materials.

Characterization

SEM images were taken by an FEI Magellan 400 XHR scanning electron microscope at an acceleration voltage of 5 kV. The elemental mapping results were analyzed by an energy-dispersive X-ray spectrometer (Bruker Quantax EBSD 400i system). Before SEM studies of cycled electrodes, batteries were disassembled in an argon-filled glovebox and then gently rinsed with DME to remove residual salt. XRD patterns were recorded on a PANalytical X'Pert instrument. XPS analysis was obtained on a PHI VersaProbe 1 scanning XPS microprobe with an air-free transfer vessel. The binding energies were calibrated with respect to the C$_{1s}$ peak at 284.6 eV. Raman spectra were produced under 532-nm laser excitation (Horiba Labram HR Evolution Raman System) at room temperature. During the self-expansion

reaction, the generated gas was collected by a sealed tube covering GoF and then injected into a gas chromatograph (SRI 8610C).

SUPPLEMENTAL INFORMATION

Supplemental Information can be found online at https://doi.org/10.1016/j.matt. 2020.04.011.

AUTHOR CONTRIBUTIONS

Y.C. conceived the idea for the project. H.C., J.W., and D.L. designed and fabricated the electrodes. H.C. conducted the SEM, Raman, and XPS characterizations. Hongxia Wang conducted the XRD characterization and gas chromatography measurements. J.W. conducted the thermal-shock reaction. S.C.K. and H.R.L. conducted the Brunauer-Emmett-Teller surface area characterizations. Z.Z. conducted the EDX characterizations. H.C. and D.B. designed and conducted the tortuosity measurements. W.H. collected the videos for USER reaction. H.C., G.Z., Hansen Wang, and Y.Y. designed and conducted the electrochemical measurements. H.C. and G.Z. carried out LiPS dissolution/diffusion loss evaluation. H.C., G.Z., D.B., D.M., and Y.C. wrote the manuscript. All authors discussed the results and commented on the manuscript at all stages.

DECLARATION OF INTERESTS

The authors declare no competing interests.

REFERENCES

1. Goodenough, J.B., and Manthiram, A. (2014). A perspective on electrical energy storage. MRS Commun. *4*, 135–142.

2. Etacheri, V., Marom, R., Elazari, R., Salitra, G., and Aurbach, D. (2011). Challenges in the development of advanced Li-ion batteries: a review. Energy Environ. Sci. *4*, 3243–3262.

3. Choi, J.W., and Aurbach, D. (2016). Promise and reality of post-lithium-ion batteries with high energy densities. Nat. Rev. Mater. *1*, 16013.

4. Manthiram, A., Fu, Y., Chung, S.H., Zu, C., and Su, Y.S. (2014). Rechargeable lithium-sulfur batteries. Chem. Rev. *114*, 11751–11787.

5. Seh, Z.W., Sun, Y., Zhang, Q., and Cui, Y. (2016). Designing high-energy lithium-sulfur batteries. Chem. Soc. Rev. *45*, 5605–5634.

6. Pang, Q., Liang, X., Kwok, C.Y., and Nazar, L.F. (2016). Advances in lithium-sulfur batteries based on multifunctional cathodes and electrolytes. Nat. Energy *1*, 16132.

7. Bruce, P.G., Freunberger, S.A., Hardwick, L.J., and Tarascon, J.M. (2012). $Li-O_2$ and Li-S batteries with high energy storage. Nat. Mater. *11*, 19–29.

8. Li, G., Wang, S., Zhang, Y., Li, M., Chen, Z., and Lu, J. (2018). Revisiting the role of polysulfides in lithium-sulfur batteries. Adv. Mater. *30*, 1705590.

9. Lin, Z., Liu, T., Ai, X., and Liang, C. (2018). Aligning academia and industry for unified battery performance metrics. Nat. Commun. *9*, 5262.

10. Liang, J., Sun, Z.-H., Li, F., and Cheng, H.-M. (2016). Carbon materials for Li-S batteries: functional evolution and performance improvement. Energy Storage Mater. *2*, 76–106.

11. Huang, S., Guan, R., Wang, S., Xiao, M., Han, D., Sun, L., and Meng, Y. (2019). Polymers for high performance Li-S batteries: material selection and structure design. Prog. Polym. Sci. *89*, 19–60.

12. Wang, L., Ye, Y., Chen, N., Huang, Y., Li, L., Wu, F., and Chen, R. (2018). Development and challenges of functional electrolytes for high-performance lithium-sulfur batteries. Adv. Funct. Mater. *28*, 1800919.

13. Lv, D., Zheng, J., Li, Q., Xie, X., Ferrara, S., Nie, Z., Mehdi, L.B., Browning, N.D., Zhang, J.-G., Graff, G.L., et al. (2015). High energy density

lithium-sulfur batteries: challenges of thick sulfur cathodes. Adv. Energy Mater. 5, 1402290.

14. Eroglu, D., Zavadil, K.R., and Gallagher, K.G. (2015). Critical link between materials chemistry and cell-level design for high energy density and low cost lithium-sulfur transportation battery. J. Electrochem. Soc. 162, A982–A990.

15. Liu, N., Zhou, G., Yang, A., Yu, X., Shi, F., Sun, J., Zhang, J., Liu, B., Wu, C.-L., Tao, X., et al. (2019). Direct electrochemical generation of supercooled sulfur microdroplets well below their melting temperature. Proc. Natl. Acad. Sci. U S A 116, 765–770.

16. Thorat, I.V., Stephenson, D.E., Zacharias, N.A., Zaghib, K., Harb, J.N., and Wheeler, D.R. (2009). Quantifying tortuosity in porous Li-ion battery materials. J. Power Sources 188, 592–600.

17. Pouraghajan, F., Knight, H., Wray, M., Mazzeo, B., Subbaraman, R., Christensen, J., and Wheeler, D. (2018). Quantifying tortuosity of porous Li-ion battery electrodes: comparing polarization-interrupt and blocking-electrolyte methods. J. Electrochem. Soc. 165, A2644–A2653.

18. Li, Y., Fu, K.K., Chen, C., Luo, W., Gao, T., Xu, S., Dai, J., Pastel, G., Wang, Y., Liu, B., et al. (2017). Enabling high-areal-capacity lithium-sulfur batteries: designing anisotropic and low-tortuosity porous architectures. ACS Nano 11, 4801–4807.

19. Chen, H., Chen, C., Liu, Y., Zhao, X., Ananth, N., Zheng, B., Peng, L., Huang, T., Gao, W., and Gao, C. (2017). High-quality graphene microflower design for high-performance Li-S and Al-ion batteries. Adv. Energy Mater. 7, 1700051.

20. Liu, Y., Zhu, Y., and Cui, Y. (2019). Challenges and opportunities towards fast-charging battery materials. Nat. Energy 4, 540–550.

21. Li, B., Li, S., Liu, J., Wang, B., and Yang, S. (2015). Vertically aligned sulfur–graphene nanowalls on substrates for ultrafast lithium-sulfur batteries. Nano Lett. 15, 3073–3079.

22. Hwa, Y., Yi, E., Shen, H., Sung, Y., Kou, J., Chen, K., Parkinson, D.Y., Doeff, M.M., and Cairns, E.J. (2019). Three-dimensionally aligned sulfur electrodes by directional freeze tape casting. Nano Lett. 19, 4731–4737.

23. Cheng, H., Ye, M., Zhao, F., Hu, C., Zhao, Y., Liang, Y., Chen, N., Chen, S., Jiang, L., and Qu, L. (2016). A general and extremely simple remote approach toward graphene bulks with in situ multifunctionalization. Adv. Mater. 28, 3305–3312.

24. Qiu, Y., Guo, F., Hurt, R., and Külaots, I. (2014). Explosive thermal reduction of graphene oxide-based materials: mechanism and safety implications. Carbon 72, 215–223.

25. Zhou, G., Yin, L.-C., Wang, D.-W., Li, L., Pei, S., Gentle, I.R., Li, F., and Cheng, H.-M. (2013). Fibrous hybrid of graphene and sulfur nanocrystals for high-performance lithium–sulfur batteries. ACS Nano 7, 5367–5375.

26. Gutiérrez, M.C., Ferrer, M.L., and del Monte, F. (2008). Ice-templated materials: sophisticated structures exhibiting enhanced functionalities obtained after unidirectional freezing and ice-segregation-induced self-assembly. Chem. Mater. 20, 634–648.

27. Zeng, Y., Li, T., Yao, Y., Li, T., Hu, L., and Marconnet, A. (2019). Thermally conductive reduced graphene oxide thin films for extreme temperature sensors. Adv. Funct. Mater. 29, 1901388.

28. Landesfeind, J., Hattendorff, J., Ehrl, A., Wall, W.A., and Gasteiger, H.A. (2016). Tortuosity determination of battery electrodes and separators by impedance spectroscopy. J. Electrochem. Soc. 163, A1373–A1387.

29. Mi, K., Chen, S., Xi, B., Kai, S., Jiang, Y., Feng, J., Qian, Y., and Xiong, S. (2017). Sole chemical confinement of polysulfides on nonporous nitrogen/oxygen dual-doped carbon at the kilogram scale for lithium–sulfur batteries. Adv. Funct. Mater. 27, 1604265.

30. Shi, F., Pei, A., Boyle, D.T., Xie, J., Yu, X., Zhang, X., and Cui, Y. (2018). Lithium metal stripping beneath the solid electrolyte interphase. Proc. Natl. Acad. Sci. U S A 115, 8529–8534.

31. Lin, D., Zhao, J., Sun, J., Yao, H., Liu, Y., Yan, K., and Cui, Y. (2017). Three-dimensional stable lithium metal anode with nanoscale lithium islands embedded in ionically conductive solid matrix. Proc. Natl. Acad. Sci. U S A 114, 4613–4618.

32. Cañas, N.A., Hirose, K., Pascucci, B., Wagner, N., Friedrich, K.A., and Hiesgen, R. (2013). Investigations of lithium–sulfur batteries using electrochemical impedance spectroscopy. Electrochim. Acta 97, 42–51.

33. Chung, S.-H., and Manthiram, A. (2019). Current status and future prospects of metal–sulfur batteries. Adv. Mater. 31, 1901125.

34. Pang, Q., Kundu, D., and Nazar, L.F. (2016). A graphene-like metallic cathode host for long-life and high-loading lithium-sulfur batteries. Mater. Horiz. 3, 130–136.

35. Zhao, X., Kim, M., Liu, Y., Ahn, H.-J., Kim, K.-W., Cho, K.-K., and Ahn, J.-H. (2018). Root-like porous carbon nanofibers with high sulfur loading enabling superior areal capacity of lithium sulfur batteries. Carbon 128, 138–146.

36. Yu, R., Chung, S.-H., Chen, C.-H., and Manthiram, A. (2018). A core-shell cathode substrate for developing high-loading, high-performance lithium–sulfur batteries. J. Mater. Chem. A 6, 24841–24847.

37. Chung, S.-H., and Manthiram, A. (2018). Rational design of statically and dynamically stable lithium–sulfur batteries with high sulfur loading and low electrolyte/sulfur ratio. Adv. Mater. 30, 1705951.

38. Chung, S.-H., Lai, K.-Y., and Manthiram, A. (2018). A facile, low-cost hot-pressing process for fabricating lithium-sulfur cells with stable dynamic and static electrochemistry. Adv. Mater. 30, 1805571.

39. Qie, L., Zu, C., and Manthiram, A. (2016). A high energy lithium-sulfur battery with ultrahigh-loading lithium polysulfide cathode and its failure mechanism. Adv. Energy Mater. 6, 1502459.

40. Yu, X., Deng, J., Lv, R., Huang, Z.-H., Li, B., and Kang, F. (2019). A compact 3D interconnected sulfur cathode for high-energy, high-power and long-life lithium-sulfur batteries. Energy Storage Mater. 20, 14–23.

41. Li, G., Lei, W., Luo, D., Deng, Y., Deng, Z., Wang, D., Yu, A., and Chen, Z. (2018). Stringed "tube on cube" nanohybrids as compact cathode matrix for high-loading and lean-electrolyte lithium–sulfur batteries. Energy Environ. Sci. 11, 2372–2381.

42. Ye, Y., Wu, F., Liu, Y., Zhao, T., Qian, J., Xing, Y., Li, W., Huang, J., Li, L., Huang, Q., et al. (2017). Toward practical high-energy batteries: a modular-assembled oval-like carbon microstructure for thick sulfur electrodes. Adv. Mater. 29, 1700598.

43. Fang, R., Zhao, S., Hou, P., Cheng, M., Wang, S., Cheng, H.-M., Liu, C., and Li, F. (2016). 3D interconnected electrode materials with ultrahigh areal sulfur loading for Li-S batteries. Adv. Mater. 28, 3374–3382.

44. Lin, D., Liu, Y., Liang, Z., Lee, H.-W., Sun, J., Wang, H., Yan, K., Xie, J., and Cui, Y. (2016). Layered reduced graphene oxide with nanoscale interlayer gaps as a stable host for lithium metal anodes. Nat. Nanotechnol. 11, 626–632.